# Journal of Materials Chemistry A

Accepted Manuscript


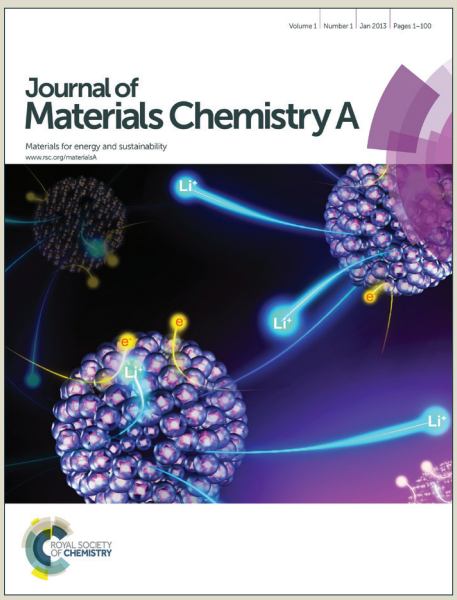





ROYAL SOCIETY OF CHEMISTRY

www.rsc.org/materialsA

Journal Name

ARTICLE

# Microfluidic generation of graphene beads for supercapacitor electrode materials

Received 00th January 20xx,
Accepted 00th January 20xx

DOI: 10.1039/x0xx00000x

www.rsc.org/

Linlin Zang,[a] Xiaojian Cao,[a] Yanhong Zhang,[b] Liguo Sun,*[b] Chuanli Qin[b] and Cheng Wang*[a]

Three-dimensional (3D) solid or hollow graphene beads (GBs) with obvious crumpled surface are fabricated by using a microfluidic emulsification device and with post-treatment process. In the emulsification process, graphene oxide (GO)/polyvinylpyrrolidone (PVP) solution is cut off by flowing dimethyl silicone oil in T-shape microfluidic channel and form into composite droplets with uniform size. PVP is used as the binder of GO sheets during the solidification and annealing procedure. The morphologies and structures of the solidified GBs are optimized by tailoring the concentration of GO/PVP solution, the size of droplets and the way of solidification. The as-prepared GBs are employed as electrode materials for supercapacitor application in this work. As three-step pre-oxidation and calcination process are carried out in the post-treatment process, the ring structure of PVP is retained and this leads to the coexistence of electric double-layer capacitance (EDLC) and pseudocapacitance property. The results show that the GBs have a specific capacitance of 243 $F \cdot g^{-1}$ at a current density of 1 $A \cdot g^{-1}$, and retain 97.5% of the initial capacitance after 3000 cycles in 6 M KOH aqueous solution. Thus, the 3D crumpled GBs present a great specific capacitance value, reduce the internal electrical resistance and enhance the durability of the electrode.

## 1. Introduction

In the past several years, due to their attractive properties of light weight, large surface area, high electrical conductivity and stable mechanical property, graphene-based assemblies and architectures, including one-dimensional fibers, two-dimensional films/papers and 3D network-structured materials, have been prepared widely via kinds of techniques.[1] Among these assemblies and architectures, 3D spherical graphene-based materials with wrinkles and ripples for providing larger accessible surface area, faster diffusion of ions and molecules, and more transport paths of electrolytes and electrons, have been widely used as the ideal supporter for electrochemical energy devices,[2-8] biological detection,[9] superhydrophobic materials,[10] catalyst,[11-13] water treatments,[14,15] and so on. Up to now, spherical graphene or their hybrid spheres have been fabricated by several methods including W/O emulsion technique,[2,3] hydrothermal process,[16,17] template assisted method,[18-27] chemical vapor deposition,[28,29] carbon source,[30-32] aerosol spray pyrolysis,[33-40] electrophoretic method[41] and so on. These methods have enriched the spherical graphene-based materials family and expanded their applications. However, these spherical graphene-based materials still had flaws, such as poor uniformity, monodispersity, spherical structure, structural hierarchy and limited means of electrochemical properties.

Here, we present novel 3D solid or hollow GBs with obvious crumpled surface by using a droplet-based microfluidic fabricating method. Because of their ability to control the structure of the final emulsion, droplet-based microfluidic techniques have paved a new way for fabrication of uniform, monodispersed, spherical beads in the micrometer to nanometer diameter, and it has become a means of constructing 3D or even more sophisticated architectures.[42-46] However, so far there have been rare reports about the fabrication of 3D spherical graphene via this way.[14,47]

In this work, we improved traditional receiving mode of droplet-based microfluidic device to fabricate 3D hollow or solid GBs. Compared with other graphene-based materials reported previous, our GBs microspheres possessed the characteristics of controllable sizes, various morphologies, well uniformity, monodispersity and sphericity. PVP was used as the binder of GO sheets. With water molecules evaporating during solidification process, water-soluble PVP diffused to the surface of composite beads to stabilize the spherical shape. Through pre-oxidation treatment and calcination process, the ring structures of PVP were partly retained, and a number of carbon nanoparticles attached to the crumpled reduced graphene oxide (rGO) sheets. The solid GBs had obvious crumpled sheets on their surfaces. When used as electrode materials, the GBs electrodes had good wettability in alkaline electrolyte and were endowed with excellent EDLC

[a] Key Laboratory of Functional Inorganic Material Chemistry (MOE), Heilongjiang University, Harbin, 150080, China. E-mail address: wangc_93@163.com
[b] Key Laboratory of Chemical Engineering Process &Technology for High-efficiency Conversion, College of Heilongjiang Province, School of Chemical Engineering and Materials, Heilongjiang University, Harbin, 150080, China. E-mail address: sunliguo1975@163.com
Electronic Supplementary Information (ESI) available: DOI: 10.1039/x0xx00000x

and pseudocapacitance property. It was demonstrated that the formation of 3D graphene sheets structure could also low diffusion resistance of ions, suppress the internal electrical resistance of the electrodes and enhance the cycle life. These features made the GBs described here ideal for electrode materials.

## 2. Experimental section

**Graphene Oxide Synthesis:** Graphene Oxide (GO) was prepared by a modified Hummers method.[48] 2 g of graphite flake was dispersed in concentrated sulfuric acid and phosphateacid (9:1, v/v) in an ice bath. 6 g potassium permanganate was slowly added and stirred the mixture for 2 h. The reaction device was subsequently transferred to a pre-heated water bath at 35 $^{o}$C and continued stirring for 24 h. 300 mL deionized water was carefully added to the reaction mixture. Then 30 mL 30% hydrogen peroxide solution was added dropwise and 5% hydrochloric acid solution (v/v) was added to remove the excess of manganese salt. The above solution was further centrifuged at 4000 rpm for 10 min to get rid of the small amount of impurities. Thus, GO solution was obtained after strong ultrasonic treatment and had a concentration of 8 mg·mL$^{-1}$.

**Preparation of graphene beads (GBs):** The schematic diagram of a modified microfluidic device to fabricate GBs was shown in Fig.1. Syringe 1 was the mixed solution of GO/PVP (3.5 g GO solution and 0.25 g PVP powder were evenly dispersed in 4 mL deionized water), and syringe 2 was dimethyl silicone oil which was used as the mobile phase. Under the shear force from mobile phase, GO/PVP droplets formed in the junction of T-shape channel. And then via a switching valve, they can be received by the mode (a) and (b). For the mode a, droplets were solidified at 60 $^{o}$C for 12 h. As for the mode b, they were heated at the same temperature for 6 h with the pear-shaped bottle rotating. Subsequently, the dry droplets were repeatedly washed with n-hexane to remove dimethyl silicone oil. The solid products were treated by three-step preoxidation process, namely, heating at 100 $^{o}$C for 2 h, 150 $^{o}$C for 10 h, and 280 $^{o}$C for 2 h in air dry oven. At last, the products were calcined at 750 $^{o}$C under $N_2$ atmosphere for 2 h.

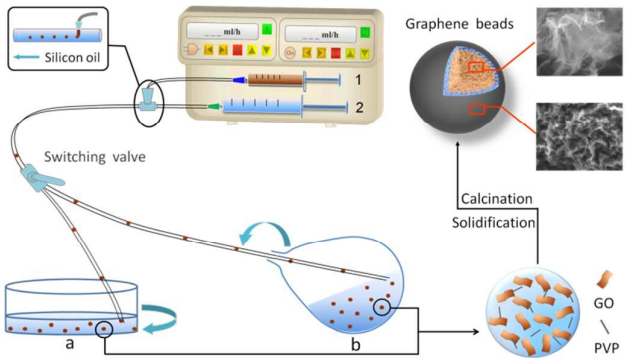


**Fig.1** Schematic diagram of a modified microfluidic device to fabricate GBs.

**Characterization:** GO was analyzed by an X-ray diffraction (XRD, BrukerD8, Cu Ka, λ = 0.15418 nm), scanning electron microscope (SEM, S-4800), transmission electron microscope (TEM, JEM-2100, JEOL, Japan) and atomic force microscopy (AFM, SPM-5100, Agilent). X-ray diffraction (XRD) patterns of GBs beads and GO were recorded with D8 ADVANCE. The morphologies and structures of GBs were examined with SEM. FT-IR spectra were obtained with ADVANCE III, and all samples were prepared by potassium bromide tabletting. X-ray photoelectron spectroscopy (XPS, AXIS Ultra DLD, Kratos) was used to clarify the chemical composition and binding energy of functional groups. Brunauer-Emmett-Teller (BET) surface area and pore size distribution measurement (ASAP 2020, surface area and pore size analyzer, Micromeritics) was carried out by nitrogen adsorption and desorption.

**Electrochemical measurements:** The electrochemical properties of the as-prepared samples were investigated with a CHI 604D electrochemical working station in 6 M KOH solution. Cyclic voltammetry (CV), galvanostatic charge/discharge (GV), and electrochemical impedance spectroscopy (EIS) techniques were conducted in a conventional three-electrode cell by the electrochemical workstation (Chenhua, Shanghai). Platinum foil and Hg/HgO electrode were used as the counter and reference electrodes, respectively. As-prepared powders were mixed with acetylene black and polytetrafluoroethylene at a mass ratio of 80:10:10 and pressed onto nickel foam (1×1 cm$^2$) to act as the working electrodes. EIS was measured at the frequencies from 100 kHz to 0.01 Hz.

## 3. Results and Discussion

### 3.1 Characteristics of GBs

Wrinkles and crumples were typical characteristics of GO. This was also observed in our work, as shown in Fig.2. In addition, the as-prepared GO sheets had also showed large and thin layer. Therefore, it was expected that they were conducive to the architecture of 3D spherical graphene.

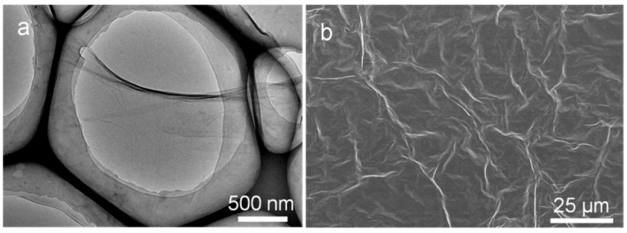


**Fig.2** (a) TEM image and (b) SEM image of GO.

As the morphologies and structures of GBs were controlled by the size of droplets, the concentration of GO/PVP solution and the way of solidification, when the size of droplets increased, the droplets started to deform under gravity and surface tension, and the shape of obtained GBs varied from sphere to

hemisphere (Fig. S1). When reducing the concentration of GO in the droplets, the excess PVP wrapped GO sheets to form hollow structure (Fig. S2). Considering the above cases, we adjusted the concentration of GO and the pushing rate ratio, 3D solid GBs with uniform sizes and stacked structure were obtained via two reception modes.

During the static solidification process, hydrophilic PVP and GO containing –COOH groups would diffused to the outer layers of droplets with water evaporating, and this led GO sheets to present inhomogeneous distribution from the inside of the droplets to the outside. Consequently, the outer rGO sheets of the GBs represented more obvious stacked structure after calcination treatment (Fig.3). In addition, carbon nanoparticles arising from carbonized PVP attached to the crumpled rGO sheets (Fig.3c), which was favorable for improving electrochemistry properties.

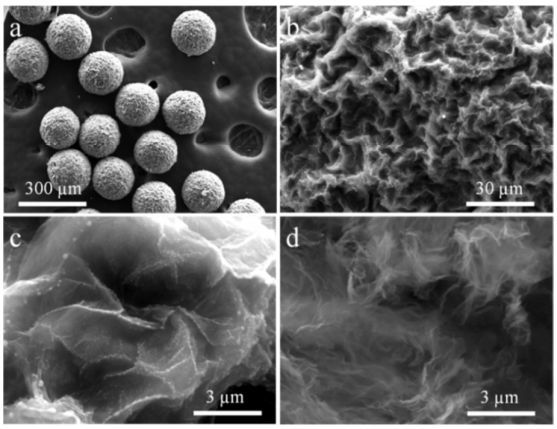


**Fig.3** SEM images of solid GBs fabricated by static solidification (mode a): (a) w (GO) = 0.45%, $v_1$: $v_2$ = 0.5:120. (b) and (c) SEM images of external surface. (d) SEM image of internal structure.

Regarding to the solidification process by the rotary evaporation method, solid GBs with closer stacked structure were obtained in shorter time (Fig.4). At the same pushing speed ratio, compared with the solid GBs in Fig.3, they had smaller average size in diameter and obvious ridged rGO sheets under the pressure force of flowing dimethyl silicone oil.

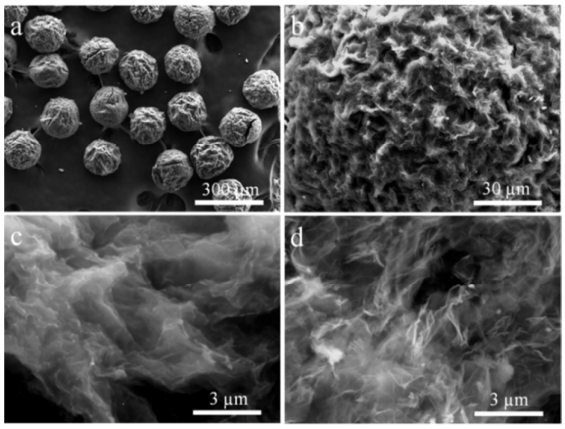


**Fig.4** SEM images of solid GBs fabricated by the rotary evaporation method (mode b): (a) $v_r$ = 200rpm, w (GO) = 0.45%, $v_1$: $v_2$ = 0.5:120. (b) and (c) SEM images of external surface. (d) SEM image of internal structure.

To further understand oxidation and reduction degree of graphene, XRD patterns were showed in Fig.S3a. A sharp diffraction peak at 11.8° demonstrated that graphite was oxidized successfully by modified Hummers method. And a broad and weak peak at 25.4° corresponded to the graphitic (002) profile, which showed the degree of crystallinity declined dramatically after GO were reduced. From the FTIR spectra (Fig. S3b), the absorption peaks of GBs were basically indentical with PVP beads, which demonstrated the presence of carbonized PVP in the GBs. Raman spectroscopy is one of effective tools to characterize the structure of carbon materials. In general, the intensity ratio of D band to G band ($I_D/I_G$) indicates the disorder degree of graphene materials. In Fig.S3c, it clearly showed that the D/G intensity ratio ($I_D/I_G$ = 0.98) of GBs was lower than that of GO ($I_D/I_G$ = 1.15), which was attributed to the reduction of GO to graphene and the improved crystallinity of GBs after carbonization treatment. The $N_2$ adsorption-desorption isotherm of the GBs was shown in Fig.S4. The isotherm curve was the type IV with a clear hysteresis loop in a wide pressure range, indicating the presence of mesoporous structure of the material. The BET surface area of the GBs by mode (a) was calculated to be 179 $m^2 \cdot g^{-1}$, which was much higher than that of graphene capsules (84 $m^2 \cdot g^{-1}$) and graphene/PANI hollow balls (103 $m^2 \cdot g^{-1}$) as reported previously.[15,19] In addition, the GBs showed an average pore size of 3.89 nm (inset of Fig.S4), which was well consistent with the SEM result (Fig.S5b). GO used in this work was characterized by AFM. The AFM image together with the height profiles in Fig.S5a clearly showed that the graphene nanosheets had a lateral dimension up to the micrometre scale and an average thickness of 1.06 nm. The SEM image of the crushed GBs was shown in Fig.S5b, which indicated the inner of them had clear porous structure and the thickness of the external surface stacked layer ranged from 6.45 to 16.13 μm.

XPS was a significant method to characterize the elemental composition of the GBs. As shown in Fig.5a, the content of nitrogen originating from the residual of PVP can be up to 5.15 at.%. The content of oxygen was 12.67 at.% and C/O ratio in rGO was much lower than the related literature,[49] which indicated that oxygen element partly arised from PVP. Those results meant that graphene beads might have two kinds of electrochemical properties, namely, EDLC and pseudocapacitance. For the C 1s XPS spectrum of the GBs (Fig.5b), four component peaks centered at 284.4, 285.1, 286.1, and 288.3 eV, which originated from C-C, C-N, C-O and C=O groups, respectively.[50] The atomic percentages of C-O and C=O indicated the existence of oxygen-containing functional groups in the GBs. Compared with GO/PVP beads, the total content of oxygen-containing functional groups in GBs decreased significantly from 42.06% to 12.67% after carbonization

treatment, and the ratio of C-OH and C=O groups decreased as well (Fig. 5a, insert table). In the case of O 1s (Fig.5c), the binding energies about 530.6, 532.2-533.5 and 535.6 eV represented C=O groups, C-OH groups and chemisorbed oxygen (carboxylic groups) and/or water, respectively.[51-55] The decomposition of PVP at above 500 °C resulted in degradation and expansion of the ring, and finally formed pyridine,[56-58] pyridine-N-oxide and pyridone-N (part of N-5). However, they were least stable at relatively intense pyrolysis conditions and converted to pyridinic-N, while pyrrolic-N (the other part of N-5) remained unaffected. Therefore, as shown in Fig.5d, the N 1s XPS spectrum of GBs was decomposed into three Gaussian peaks with their binding energy of 398.1, 400.5 and 404.3 eV, assigned to pyridinic (N-6), pyrrolic/pyridone (N-5) and pyridine-N-oxide (N-X), respectively.[58-60]

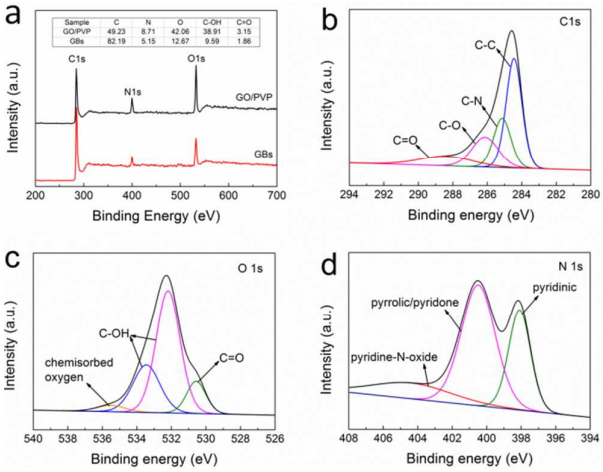


**Fig. 5** (a) XPS of GO/PVP and GBs (insert table was the content (%) of C, N, O, C-OH and C=O in GO/PVP and GBs, respectively). (b), (c) and (d) were C 1s, O 1s, N 1s spectra of GBs (prepared by mode (a), and w (GO) = 0.45%, $v_1$: $v_2$ = 0.5:120), respectively.

### 3.2 Electrochemical performance

The GBs received via the mode (a) were utilized as electrodes materials and their electrochemical properties were performed. Fig.6a showed the CV curves of GBs and PVP beads at scan rate of 10 mV·s$^{-1}$ in the potential range of -0.2 to 0.6 V. During the testing process, nearly rectangular shape and obvious redox peaks of the curves indicated the coexistence of EDLC and pseudocapacitance properties. It was because that the GBs electrode materials existed charge transfer in the ring structure arising from PVP, which led to pseudocapacitance property and unsymmetrical redox peaks. It was also noted that GBs electrode possessed apparently larger specific capacitance, which attributed to their 3D structure and highly electroactive regions. Fig.6b showed the CV curves of GBs electrode at scan rates of 5-100 mV·s$^{-1}$. It can be seen that the oxidation peaks shifted positively and the reduction peaks shifted negatively with increasing scan rate, which is mainly due to the resistance of the electrode.[61] Fig.6c showed the GV curves of GBs and PVP beads electrodes at a constant current density of 1 A·g$^{-1}$. Because of pseudocapacitors behavior, both GV curves displayed a bent triangular shape. It can be also observed that a voltage drop existed at the beginning of the discharge curve, and the IR drop of GBs was significantly lower than that of PVP beads. These results indicated that the 3D graphene sheets effectively suppressed the internal electrical resistance of the electrodes.[62] Fig.6d represented the GV curves of GBs at current densities of 0.5, 1, 2, 3 and 5 A·g$^{-1}$ and the specific capacitances were 248, 243, 227, 183 and 176 F·g$^{-1}$, respectively.

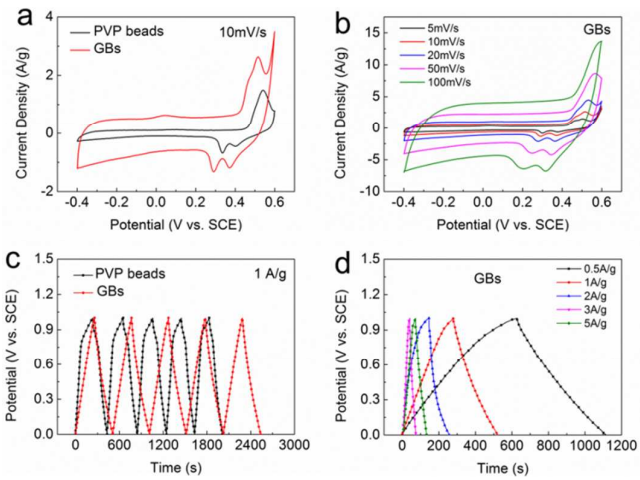


**Fig.6** (a) CV curves of GBs (prepared by mode (a), and w (GO) = 0.45%, $v_1$: $v_2$ = 0.5:120) and PVP beads at 10 mV·s$^{-1}$. (b) CV curves of GBs electrode at 5-100 mV·s$^{-1}$. (c) GV curves of GBs and PVP beads electrodes at 1 A·g$^{-1}$. (d) GV curves of GBs at 0.5-5 A·g$^{-1}$.

In order to investigate the durability of the electrode materials, a repetitive charge-discharge cycling test was carried out at a current density of 1 A·g$^{-1}$ (Fig.7). The specific capacitance retention ratios of GBs and PVP beads electrodes were 97.5% and 89.7% after 3000 cycles, respectively, demonstrating that GBs electrode possessed better long-term electrochemical stability and did not bring in a significant structural change after a repeated charge/discharge test. These results revealed that the cycle life could be enhanced by the formation of 3D graphene sheets structure.[63]

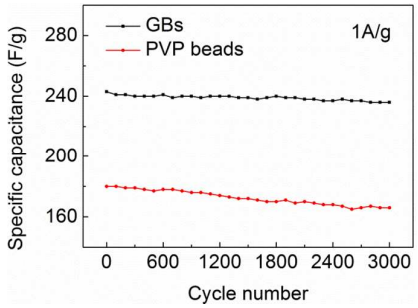


**Fig.7** Charge–discharge cycling test of GBs (prepared by mode (a), and w (GO) = 0.45%, $v_1$: $v_2$ = 0.5:120) and PVP beads electrodes at 1 A·g$^{-1}$.

To understand the dielectric and transport properties of the electrodes, EIS was conducted for PVP beads and GBs electrodes (Fig.8). It is well-known that ideal electrochemical capacitance behavior exhibits a small depressed semicircle at high frequency and the imaginary part of the impedance in the low frequency region being perpendicular to the real part.[64] An intercept of the semicircle at the x-axis (starting point) represents internal resistance (*Rs*) and it corresponds to the internal charge, charge/discharge rate, and wettability of the electrode.[65,66] It was observed that *Rs* of PVP beads and GBs were 1.49 and 0.94 Ω, respectively. The smaller *Rs* value of the GBs electrode may result from the formation of 3D graphene structure where efficient access of electrolyte ions can be facilitated inside the 3D sheets structure to the electrode surface and shorten the ion diffusion path. The obvious difference in the diameter of the semicircles indicated that GBs had much lower resistance in charge propagation at the interface between the electrode/electrolyte than the PVP beads. And GBs electrode exhibited a more vertical line than PVP beads electrode at low frequency, demonstrating better capacitive behavior and lower diffusion resistance of ions. In addition, we also investigated the electrochemical performance of GBs with different GO content, the size of droplets and the pushing rate ratio. The CV, GV and charge-discharge cycling tests were shown in Fig.S8 and Table S1.

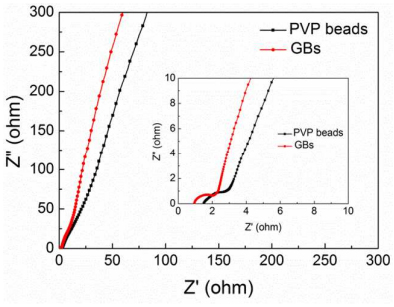


**Fig.8** Nyquist plots for PVP beads and GBs (prepared by mode (a), and w (GO) = 0.45%, $v_1$: $v_2$ = 0.5:120) electrodes.

## 4. Conclusion

We successfully prepared 3D GBs via a modified microfluidic device. In this process, a small amount of PVP was used as the binder of GO sheets to keep the solid sphericity. Through controlling the sizes of droplets, adjusting the concentration of GO solution and choosing the receiving methods, solid or hollow GBs can be obtained successfully. As for the solid GBs, their internal and external rGO sheets represented significant wrinkled structure, and a number of carbon nanoparticles originating from the calcination of PVP attached to external rGO sheets. When used as electrode materials for supercapcitor, these solid GBs exhibited the coexistence of EDLC and pseudocapacitance, which showed a specific capacitance of 243 $F \cdot g^{-1}$ at a current density of 1 $A \cdot g^{-1}$ and retained 97.5% of the initial capacitance after 3000 cycles in 6 M KOH aqueous solution.

## Acknowledgements

The present study has been supported by NSFC (51273056, 51473046, 21202091, 51303045, 21206034 and 51372072), HLJNSF of Heilongjiang (1254-NCET-024), Abroad Person with Ability Foundation of Heilongjiang Province (11551339, 12521400 and 1252CGZH09), China postdoctoral science foundation (2014M561545), Heilongjiang Province Postdoctoral Science Foundation (LBH-Q12021 and LBH-Q09032) and Heilongjiang Provincial Department of Education (12531521).

## Notes and references

1 H. P. Cong, J. F. Chen and S. H. Yu, *Chem. Soc. Rev.*, 2014, **43**, 7295-7325.
2 R. R. Yao, D. L. Zhao, L. Z. Bai, N. N. Yao and L. Xu, *Nanoscale Res. Lett.,* 2014, **9**, 1-6.
3 P. Guo, H. H. Song and X. H. Chen, *J. Mater. Chem.*, 2010, **20**, 4867-4874.
4 J. Y. Cao, Y. M. Wang, P. Xiao, Y. C. Chen, Y. Zhou, J. H. Ouyang and D. C. Jia, *Carbon*, 2013, **56**, 389-391.
5 D. D. Cai, L. X. Ding, S. Q. Wang, Z. Li, M. Zhu and H. H. Wang, *Electrochim. Acta*, 2014, **139**, 96-103.
6 M. Z. Ge, S. H. Li, J. Y. Huang, K. Q. Zhang, S. S. Al-Deyab and Y. K. Lai, *J. Mater. Chem. A*, 2015, **3**, 3491-3499.
7 H. W. Wang, C. Guan, X. F. Wang and H. J. Fan, *Small*, 2015, **11**, 1470-1477.
8 S. H. Yang, X. F. Song, P. Zhang, J. Sun and L. Gao, *Small*, 2014, **10**, 2270-2279.
9 H. J. Zhang, P. B. Gai, R. Cheng, W. Liang, X. H. Zhang and J. H. Chen, *Anal. Methods*, 2013, **5**, 3591-3600.
10 J. S. Lee, J. C. Yoon and J. H. Jang, *J. Mater. Chem. A*, 2013, **1**, 7312-7315.
11 W. G. Tu, Y. Zhou, Q. Liu, Z. P. Tian, J. Gao, X. Y. Chen and Z. G. Zou, *Adv. Funct. Mater.*, 2012, **22**, 1215-1221.
12 L. F. Wu, H. B. Feng, M. J. Liu, K. X. Zhang and J. H. Li, *Nanoscale*, 2013, **5**, 10839-10843.
13 B. Zeng, X. H. Chen, Y. X. Luo, Q. Y. Liu and W. Z. Zeng, *Ceram. Int.*, 2014, **40**, 5055-5059.
14 J. Wang, L. R. Shang, Y. Cheng, H. B. Ding, Y. J. Zhao and Z. Z. Gu, *Small*, 2015, DOI: 10.1002/smll.201500691.
15 K. Sohn, Y. J. Na, H. K. Chang, K. M. Roh, H. D. Jang and J. X. Huang, *Chem. Commun.*, 2012, **48**, 5968-5970.
16 W. D. Xue, R. Zhao, X. Du, F. W. Xu, M. Xu and K. X. Wei, *Mater. Res. Bull.*, 2014, **50**, 285-291.
17 Y. Wang, J. Y. Cao, J. C. Rao, X. X. Lu, P. Xiao and Y. Zhou, *RSC Adv.*, 2014, **4**, 5826-5829.
18 Q. G. Shao, J. Tang, Y. X. Lin, F. F. Zhang, J. S. Yuan and L. C. Qin, *J. Mater. Chem.*, A 2013, **1**, 15423-15428.
19 N. B. Trung, V. T. Tam, H. R. Kim, S. H. Hur, E. J. Kim and W. M. Choi, *Chem. Eng. J.*, 2014, **255**, 89-96.
20 H. Wang, L. Y. Shi, T. T. Yan, J. P. Zhang, Q. D. Zhong and D. S. Zhang, *J. Mater. Chem. A*, 2014, **2**, 4739-4750.
21 J. Zhang, Y. Yu, L. Liu and Y. Wu, *Nanoscale*, 2013, **5**, 3052-3057.
22 W. Fan, C. Zhang, W. W. Tjiu, K. P. Pramoda, C. B. He and T. X. Liu, *ACS appl. Mater. Inter.*, 2013, **5**, 3382-3391.
23 S. A. Ju, K. Kim, J. H. Kim and S. S. Lee, *ACS appl. Mater. Inter.*, 2011, **3**, 2904-2911.

24 M. Li, Y. Q. Zhang, L. L. Yang, Y. K. Liu and L. S. Yao, *Electrochim. Acta*, 2015, **166**, 310-319.
25 C. X. Guo and C. M. Li, *Energ. Environ. Sci.*, 2011, **4**, 4504-4507.
26 J. W. Liu, Q. Zhang, X. W. Chen and J. H. Wang, *Chem. Eur. J.*, 2011, **17**, 4864-4870.
27 M. Shahid, N. Yesibolati, M. C. Reuter, F. M. Ross and H. N. Alshareef, *J. Power Sources*, 2014, **263**, 239-245.
28 R. Atchudan, A. Pandurangan and J. Joo, *Micropor. Mesopor. Mat.*, 2013, **175**, 161-169.
29 J. S. Lee, S. I. Kim, J. C. Yoon and J. H. Jiang, *ACS Nano*, 2013, **7**, 6047-6055.
30 X. J. He, H. B. Zhang, H. Zhang, X. J. Li, N. Xiao and J. S. Qiu, *J. Mater. Chem. A*, 2014, **2**, 19633-19640.
31 S. M. Yoon, W. M. Choi, H. Baik, H. J. Shin, I. Song, M. S. Kwon and J. Y. Choi, *ACS Nano*, 2012, **6**, 6803-6811.
32 S. G. Lee, J. Hong, J. H. Koo, H. Lee, S. Lee, T. J. Choi and T. Lee, *ACS appl. Mater. Inter.*, 2013, **5**, 2432-2437.
33 L. Song, S. N. Lim, K. K. Kang and S. B. Park, *J. Mater. Chem. A*, 2013, **1**, 6719-6722.
34 J. Y. Luo, H. D. Jang, T. Sun, L. Xiao, Zhen. He and M. G. Kanatzidis, *ACS Nano*, 2011, **5**, 8943-8949.
35 J. Y. Luo, H. D. Jang and J. X. Huang, *ACS Nano*, 2013, **7**, 1464-1471.
36 S. H. Choi and Y. C. Kang, *Carbon*, 2014, **79**, 58-66.
37 S. H. Choi and Y. C. Kang, *Chem. Eur. J.*, 2014, **20**, 6294-6299.
38 X. L. Chen, G. Wu, T. Lan and W. Chen, *Chem. Commun.*, 2014, **50**, 7157-7159.
39 S. H. Choi, Y. N. Ko, J. K. Lee and Y. C. Kang, *Sci. Rep.*, 2014, **4**.
40 S. Mao, Z. H. Wen, Z. Bo, J. B. Chang, X. K. Huang and J. H. Chen, *ACS appl. Mater. Inter.*, 2014, **6**, 9881-9889.
41 X. Zhang, Y. K. Lai, M. Z. Ge, Y. X. Zheng, K. Q. Zhang and Z. Q. Lin, *J. Mater. Chem. A*, 2015, **3**, 12761-12768.
42 X. T. Sun, M. Liu and Z. R. Xu, *Talanta,* 2014, **121**, 163-177.
43 Y. Cheng, F. Y. Zheng, J. Lu, Z. Y. Xie, Y. J. Zhao, Y. P. Cheng and Z. Z. Gu, *Adv. Mater.*, 2014, **26**, 5184-5190.
44 Y. J. Zhao, Y. Cheng, L. R. Shang, J. Wang, Z. Y. Xie and Z. Z. Gu, *Small*, 2015, **11**, 151-174.
45 L. R. Shang, F. Q. Shangguan, Y. Cheng, J. Lu, Z. Y. Xie, Y. J. Zhao and Z. Z. Gu, *Nanoscale*, 2013, **5**, 9553-9557.
46 L. R. Shang, Y. Cheng, J. Wang, H. B. Ding, F. Rong, Y. J. Zhao and Z. Z. Gu, *Lab on a Chip*, 2014, **14**, 3489-3493.
47 D. J. Han, J. H. Jung, J. S. Choi, Y. T. Kim and T. S. Seo, *Lab on a Chip*, 2013, **13**, 4006-4010.
48 D. C. Marcano, D. V. Kosynkin, J. M. Berlin, A. Sin itskii, A. Slesarev and J. M. Tour, *ACS Nano*, 2010, **4**, 4806-4814.
49 S. F. Pei and H. M. Cheng, *Carbon*, 2012, **50**, 3210-3228.
50 H. Peng, G. F. Ma, K. J. Sun, J. J. Mu, M. T. Luo and Z. Q. Lei, *Electrochim. Acta*, 2014, **147**, 54-61.
51 E. Desimoni, G. I. Casella, T. R. Cataldi and A. M. Salvi, *Surf. Interface Anal.*, 1992, **18**, 623-630.
52 A. Proctor and P. M. Sherwood, *Carbon*, 1983, **21**, 53-59.
53 H. Darmstadt, C. Roy and S. Kaliaguine, *Carbon*, 1994, **32**, 1399-1406.
54 C. Kozlowski and P. M. Sherwood, *Carbon*, 1986, ***24***, 357-363.
55 F. Atamny, J. Blöcker, A. Dübotzky, H. Kurt, W. Mahdi and R. Schlögl, *Mol. Phys,*. 1992, ***76***, 851-886.
56 I. A. Jacobson, H. H. Heady and G. U. Dinneen, *J. Phys. Chem.lett.*, 1958, ***62***, 1563-156.
57 J. M. Patterson and P. Drenchko, *J. Org. Chem.*, 1962, **27**, 1650-1652.
58 J. R. Pels, F. Kapteijn, J. A. Moulijn, Q. Zhu and K. M. Thomas, *Carbon*, 1995, **33**, 1641-1653.
59 C. O. Ania, V. Khomenko, E. Raymundo-Piñero, L. B. Parra and F. Beguin, *Adv. Funct. Mater.*, 2007, **17**, 1828-1836.
60 S. Biniak, G. Szymański, J. Siedlewski and A. Światkowski, *Carbon*, 1997, **35**, 1799-1810.
61 J. Li, H. Q. Xie, Y. Li, J. Liu and Z. X. Li, *J. Power Sources*, 2011, **196**, 10775-10781.
62 Z. Zhou and X. F. Wu, *J. Power Sources*, 2013, **222**, 410-416.
63 N. B.Trung, Tam. T. Van, H. R. Kim, S. H. Hur, E. J. Kim, W. M. Choi and *Chem. Eng. J.*, 2014, **255**, 89-96.
64 L. Q. Fan, G. J. Liu, J. H. Wu, L. Liu, J. M. Lin and Y. L. Wei, *Electrochim. Acta*, 2014, **137**, 26-33.
65 L. P. Zheng, Y. Wang, X. Y. Wang, H. F. An and L. H. Yi, *J. Mater. Sci.*, 2010, **45**, 6030-6037.
66 Y. Wang, Z. Q. Shi, Y. Huang, Y. F. Ma, M. M. Chen and Y. S. Chen, *J. Phys. Chem. C*, 2009, **113**, 13103-13107.

Three-dimensional (3D) solid or hollow graphene beads (GBs) with obvious crumpled surface were fabricated by a microfluidic emulsification device and employed as electrode materials for supercapacitor.